Journal of Sound and Vibration 514 (2021) 116443

Contents lists available at ScienceDirect

Journal of Sound and Vibration

journal homepage: www.elsevier.com/locate/jsvi

Experimental study on active tuned inerter-dampers: Application to active damping using force feedback

Guoying Zhao, PhD [a,*], Ahmad Paknejad [b], Ghislain Raze [c], Arnaud Deraemaeker [d], Gaetan Kerschen [c], Christophe Collette [b,c]

[a] TianQin Research Centre for Gravitational Physics, Sun Yat-Sen University, No.2 Daxue Rd., Zhuhai 519082, China
[b] Precision Mechatronics Laboratory, Beams Department, Université Libre de Bruxelles, F.D.Roosevelt Av 50, Brussels 1050, Belgium
[c] Department of Aerospace and Mechanical Engineering, University of Liège, Allée de la Découverte 9, Liège 4000, Belgium
[d] BATir Department, Université Libre de Bruxelles, F.D.Roosevelt Av 50, Brussels 1050, Belgium

ARTICLE INFO

Keywords:
Inerter
H-infinity optimisation
Force feedback
Active damping

ABSTRACT

In this paper, a modified active tuned inerter damper concept which is more suitable for practical applications is proposed. The proposed device is composed of a pair of collocated reactive actuator and force sensor. A second-order low-pass filter and a proportional term are combined to form the controller. The equivalent mechanical model of the controller's components is derived in order to better interpret the coupled system. The second-order low-pass filter is mechanically equivalent to a pure mechanical network which comprises an inerter, a spring and a damper connected in parallel. The proportional term mechanically represents a spring which is connected in series with the inherent actuator spring. Simple regressions are derived based on the $\mathbb{H}_\infty$ optimisation criterion wherein the optimal feedback gains are calculated to minimise the maximal response of the driving-point receptance of the system. The numerical study is also experimentally validated. The obtained results are found to correspond well with the theoretical developments.

1. Introduction

Lightweight materials and monolithic design concepts have been more and more employed in the new designs of structures for the sake of reduction of environmental pollution and ultra-performance [1,2]. However, this will often make these structures lightly-damped and thus more prone to vibrations, which could cause many problems such as reduction in structural integrity, compromise of instrument functionality and even threat to human lives. In this regard, proper damping techniques need to be considered in parallel with the future design of lightweight structures. Vibration absorbers, especially tuned mass dampers (TMDs) are often used for such purpose [3–7]. A TMD typically consists of a proof mass and a spring-dashpot pair added to the primary structure as an auxiliary system [8]. Once it is properly tuned, the vibration energy of the primary structure can be quickly transferred to the TMD where it is eventually dissipated. The damping effectiveness is known to ultimately depend on the weight of its proof mass, where better control performance comes with a heavier proof mass. However, the added mass may be penalising in lightweight applications.

One interesting solution to address this trade-off is to use inerters. An inerter is defined as a one-port mechanical element which impedes the relative acceleration across its terminals [9,10]. Inerters became more and more attractive in the field of mechanical

---

[*] Corresponding author.
E-mail address: zhaoguoying@mail.sysu.edu.cn (G. Zhao).

https://doi.org/10.1016/j.jsv.2021.116443
Received 26 March 2021; Received in revised form 17 August 2021; Accepted 7 September 2021

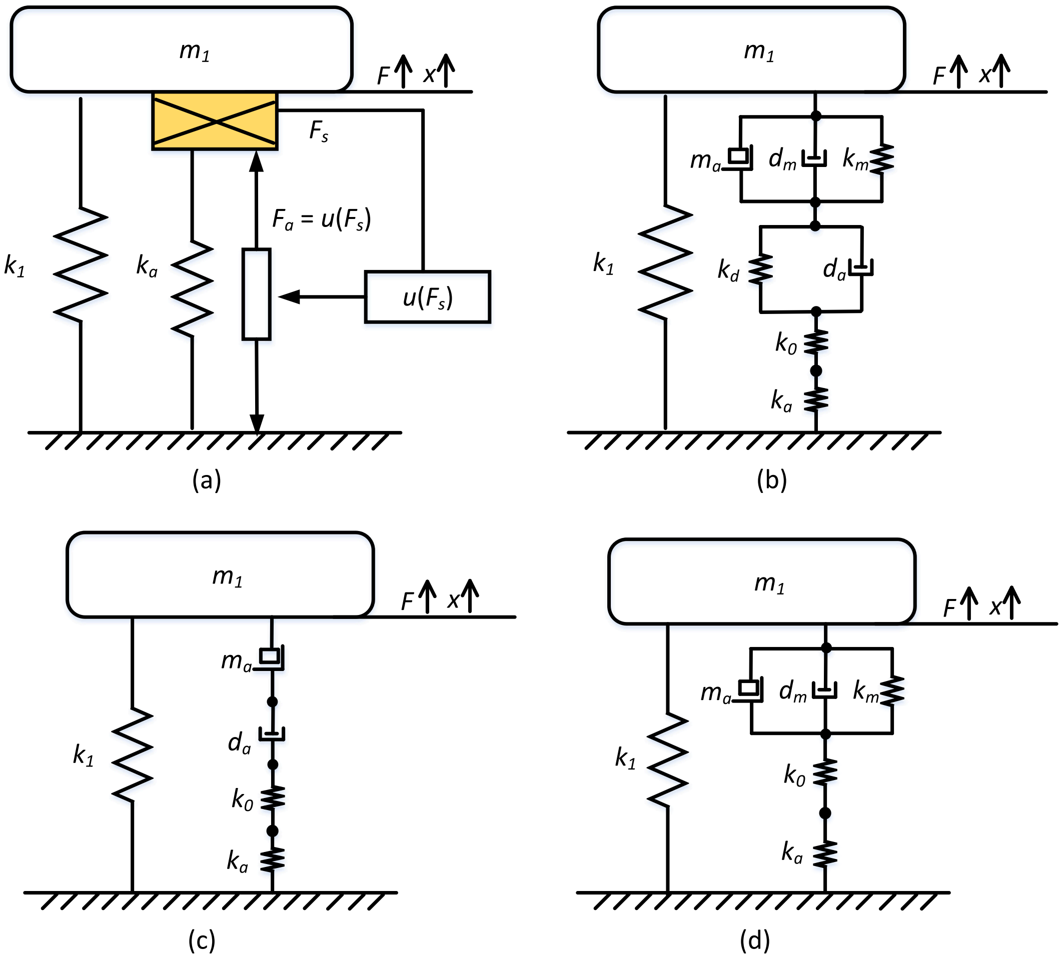

Fig. 1. (a) The schematics of the system under investigation, (b) the equivalent mechanical model (practical ATID-S), (c) the ideal ATID-S and (d) the ATID-P.

vibration suppression because their inertance (representing the impedance coefficient in kilograms) can be significantly greater than their actual mass [9]. This interesting feature inspired many new design concepts aiming to outperform traditional TMDs. These include tuned inerter-damper (TID) which is similar to TMD but using inerters to replace the proof mass of TMDs, and tuned mass-damper-inerter (TMDI) which directly integrates inerters into TMDs [11–13]. For these systems, the actual mass is lower than the effective proof mass added to a primary structure, thus boosting the vibration mitigation performance while preserving the lightweight feature of the vibration absorber.

Inerters have also been found to be useful for active vibration absorbers [14,15]. For example, Zilletti [16] proposed to include an inerter in parallel with the suspension system of the active vibration absorber with the aim to reduce the natural frequency of the active device without overly increasing the actual weight. Consequently, this improves the stability margin and the control bandwidth of the traditional active vibration absorbers. Alujevic et al. [17] investigated the potential of a novel inerter-based active vibration isolation system. The authors have shown that adding the inerter into the isolator can effectively stabilise the conditionally stable control loop thus allowing to further increase the loop gain.

Although these inerter based designs are promising, it is quite challenging to realise them in practice because some imperfections during the mechanical construction will be inevitably present, preventing them to act as idealised inerters. For instance, the performance of ball-screw and rack-pinion inerters may degrade because of the friction and backlash or elastic effect of gears and screws [18], and hydraulic inerters may exhibit nonlinear damping in addition to the inertance-like behaviour [19].

In order to bypass the problems associated with physical inerters, the potential of active inerter-based vibration absorbers was investigated. It was reported that active inerter-based vibration absorbers can be implemented by a pair of collocated reactive actuator and force sensor. By feeding back the output of the force sensor through a resonant controller [20] or a sum of single and double integrators [21–23] to drive the actuator, the inerter can be synthetised, resulting in systems equivalent to mechanical networks composed of a spring, dashpot and inerter connected in parallel or in series, respectively. However, the experimental validation is not yet available, and it still remains challenging to achieve an acceptable control performance when targeting for high-order modes of the primary structure. This is because the dynamic stiffness ratio between the actuator and the primary structure ultimately determines the achievable control performance of these strategies and this ratio decreases at high frequencies.

The focus of this study is thus twofold: (1) to develop a modified force feedback controller which allows to further boost the control performance and (2) to experimentally investigate the potential of the proposed controller. The proposed controller is built upon our previous developments [23]. A proportional term is added to the original controller which opens the possibility to tune the effective stiffness of the actuator. On top of this, a simple second-order low-pass filter is used to replace the pure integrators in the original controller which helps suppress the very pronounced saturation problems for example caused by the low-frequency drift of the instrument in practical applications. The $\mathbb{H}_\infty$ optimisation criterion is utilised to calculate the optimal parameters of the proposed controller and a fitting technique is employed to establish the dependence of the control parameters on the fixed system parameters. The mechanical equivalence of the components in the proposed controller is also explicitly discussed in order to provide more physical insights. Experimental validations are provided which verify the theoretical analysis. The presented experimental work also aims to pave the way for the examination of previous analytical works on active nonlinear inerter-based dampers [24,25].

The paper is structured into four sections. In the Section 2, the mathematical models are presented, based on which the optimal feedback gains for implementing the controller are derived. In Section 3, experimental results are presented for the validation of the numerical study. The conclusions are drawn in Section 4.

2. Mathematical modelling and parameter optimisation

2.1. Mathematical modelling

The system under investigation is shown in Fig. 1 (a). It represents an undamped single-degree-of-freedom (SDOF) system which is equipped with a massless actuator whose stiffness is denoted by k_a. The SDOF system is defined through the mass m_1 and the suspension stiffness k_1. It is excited by a disturbance force F. A collocated force sensor which measures the transmission force F_s is installed between the actuator and the primary structure. The control loop is implemented by feeding the output of the force sensor F_s through a controller $u(F_s)$ to drive the actuator.

The governing equations of the coupled system can be written as:

$$m_1\ddot{x}(t) + k_1x(t) = F(t) + F_s(t) \tag{1}$$

$$F_s(t) = u(F_s(t)) - k_ax(t) \tag{2}$$

An active inerter-damper control concept was proposed in the previous study [23], where the controller $u(F_s) = -g_s\int_0^t F_s(t)\mathrm{d}t - g_d\int_0^t\int_0^t F_s(t)\mathrm{d}t\mathrm{d}t$ is used. However, pure integrators cannot be applied in practice for control in some cases as they might lead to saturation problems due to the undesirable amplification of the control signal at low frequencies. Thus, the controller $u(F_s(t))$ is modified as:

$$u(F_s(t)) = -g_sL_1(F_s(t)) - g_dL_2(F_s(t)) - g_0F_s(t) \tag{3}$$

where $L_1(\bullet)$ and $L_2(\bullet)$ represent a first and a second order low-pass filter, respectively. g_s, g_d and g_0 are the control gains.

Transforming Eq. (3) into Laplace domain, one obtains:

$$U(F_s(s)) = -g_s\frac{F_s(s)}{s+a} - g_d\frac{F_s(s)}{(s+a)^2} - g_0F_s(s) \tag{4}$$

where a is the corner frequency of the low-pass filters and s represents the Laplace variable.

Compared with the controller studied in Zhao et al. [23], the single and double integrators are now replaced by first and second order low-pass filters, respectively. In this way, the saturation problems can be limited. The proportional term in Eq. (4) is introduced in order to be able to tune the effective stiffness of the actuator. This can be better understood from a pure mechanical point of view. The equivalent mechanical representation of the considered system is shown in Fig. 1 (b). The proof is provided in Appendix A. As can be seen, the control effect of the proportional term $g_0F_s(s)$ is equivalent to placing a spring in series with the inherent spring of the actuator. Combining them, the effective stiffness of the actuator, denoted by $k_a^{'}$, can be derived:

$$k_a^{'} = \frac{k_a}{1+g_0} \tag{5}$$

When the gain g_0 is positive, the equivalent stiffness $k_a^{'}$ is reduced as two positive springs are connected in series. On the other hand, $k_a^{'}$ is increased assuming $-1 < g_0 < 0$, which actually favours the vibration mitigation performance as demonstrated in Zhao et al. [23]. The underlying idea is similar to the concept of shunting negative capacitors to piezoelectric elements, thanks to which the generalised electromechanical coupling factor can be boosted leading to a better vibration mitigation performance [26–29].

As can be also seen in Fig. 1 (b), the use of the first-order and second-order low-pass filters introduces a spring k_d and a pair of spring and dashpot $k_m$and $d_m$in addition to the desired dashpot d_a and inerter m_a. Although the saturation problems can be suppressed by the proposed controller, the complexity on the control parameter optimisation is increased.

The equivalent damping coefficient d_m and d_a, the inertance m_a and the stiffness k_d, $k_m$and $k_0$can be linked with the control parameters according to:

$$d_a = \frac{k_a}{g_s}, d_m = \frac{2ak_a}{g_d}, m_a = \frac{k_a}{g_d}, k_d = \frac{ak_a}{g_s}, k_m = \frac{a^2 k_a}{g_d}, k_0 = \frac{k_a}{g_0} \tag{6}$$

Note that the corner frequency related parameters k_d, k_m and d_m go to zero when the corner frequency a is set to zero.

In order to come to a more general formulation, the following parameters:

$$\begin{aligned} &\tau = \omega_1 t, \quad x_1 = x, \quad x_2 = F_s/k_1, \quad x_d = F/k_1, \quad \omega_1 = \sqrt{k_1/m_1}, \\ &\Omega_c = \frac{a}{\omega_1}, \quad \mu = \frac{k_a}{(1+g_0)k_1}, \quad g_{dn} = \frac{g_d}{(1+g_0){\omega_1}^2}, \quad g_{sn} = \frac{g_s}{(1+g_0)\omega_1} \end{aligned} \tag{7}$$

are introduced to normalise the system governing Eqs. (1) and (2):

$$\ddot{x}_1 + x_1 - x_2 = x_d \tag{8}$$

$$\ddot{x}_2 + (2\Omega_c + g_{sn})\dot{x}_2 + \left({\Omega_c}^2 + g_{dn} + g_{sn}\Omega_c\right)x_2 + \mu\left(\ddot{x}_1 + 2\Omega_c\dot{x}_1 + {\Omega_c}^2 x_1\right) = 0 \tag{9}$$

where the derivatives are calculated with respect to the time scale τ as defined in Eq. (7).

Considering now the pure integrators are used i.e. Ω_c is set to zero in Eq. (9), the corresponding schematic of the equivalent mechanical model can be derived as shown in Fig. 1 (c) which actually represents a TID with its components connected in series. In practical applications, low-pass filters have to be used to replace the pure integrators. The corner frequency of the low-pass filters is often configured relatively low compared with the resonance to be damped. This makes the extra components related to the corner frequency of the low-pass filters vaguely present in the network. Thus, the whole network still behaves as its ideal case i.e. an ATID. Based upon this, the abbreviation ATID-S is chosen to address the schematic shown in Fig. 1(b). 'S' in this case is referred to as a serial connection of the inerter and the dashpot.

As stated earlier, a second-order low-pass filter already introduces an additional pair of spring and dashpot. It was found that the inclusion of a first-order low-pass filter exhibits no better results than a second-order low-pass filter alone in terms of the control performance as shown later in Fig. 5 and the stability concern as discussed in Appendix B. Therefore, the term associated with g_{sn} is eliminated from the controller in Eq. (9) which then becomes:

$$\ddot{x}_2 + 2\Omega_c\dot{x}_2 + \left({\Omega_c}^2 + g_{dn}\right)x_2 + \mu\left(\ddot{x}_1 + 2\Omega_c\dot{x}_1 + {\Omega_c}^2 x_1\right) = 0 \tag{10}$$

In such a scenario, the corresponding equivalent mechanical network, as shown in Fig. 1 (d), essentially becomes a parallel connection of an inerter, dashpot and spring (induced by the second-order low-pass filter) which is then connected in series with another spring (corresponding to the proportional term). This modified controller is referred to as ATID-P which stands for an active tuned inerter damper in which the inerter, the spring and the dashpot are connected in parallel.

2.2. Parameters optimisation

The $\mathbb{H}_\infty$ norm is employed to optimise the control parameters of the proposed controller. The magnitude of the normalised driving-point receptance $|x_1/x_d|$ is taken as the performance index.

The normalised driving-point receptance of the primary structure can be derived according to Eqs. (8) and (9):

$$\frac{x_1}{x_d} = \frac{S^2 + 2\Omega_c S + {\Omega_c}^2 + g_{dn}}{S^4 + 2\Omega_c S^3 + \left(1 + {\Omega_c}^2 + g_{dn} + \mu\right)S^2 + 2\Omega_c(\mu+1)S + {\Omega_c}^2(\mu+1) + g_{dn}} \tag{11}$$

and its magnitude is given as:

$$\left|\frac{x_1}{x_d}\right| = \frac{\sqrt{\Omega^4 + \left(2{\Omega_c}^2 - 2g_{dn}\right)\Omega^2 + \left({\Omega_c}^2 + g_{dn}\right)^2}}{\sqrt{2\mu\left(\Omega^2 - 1\right)\left(\left(\Omega^2 - {\Omega_c}^2\right)g_{dn} - \left(\Omega^2 + {\Omega_c}^2\right)\left(\Omega^2 + {\Omega_c}^2\right)\right) + \left(\Omega^2 - 1\right)^2 C + D}} \tag{12}$$

where $C = (g_{dn})^2 + (-2\Omega^2 + 2{\Omega_c}^2)g_{dn} + (\Omega^2 + {\Omega_c}^2)^2$, $S = s/\omega_1$ is the normalised Laplace variable, $\Omega = S/j$ is the normalised frequency and $D = (\Omega^2 + {\Omega_c}^2)^2\mu^2$.

The optimisation parameters could in principle be any of the three in Eq. (12), but the stiffness ratio μ is often constrained by the requirements on the change of the structure's dynamics due to the installation of the active damping device and is thus considered as fixed. Therefore, the remaining optimisation parameters are the normalised feedback gains g_{dn} and the cut-off frequency Ω_c. Because explicit expressions for their optimal values are very complicated to obtain, a numerical $\mathbb{H}_\infty$ optimisation (a gradient-based method implemented in MATLAB function *fminsearch*) is performed instead where optimal values of g_{dn} and Ω_c are sought to minimise the resonance peaks for a fixed stiffness ratio μ. This procedure is repeated for a large variation of μ ($0 < \mu \leq 1.5$) and then a fitting technique is employed to establish the dependence of g_{dn} and Ω_c on μ. It turns out that the following regressions provide an excellent

Table 1
Goodness of fitting.

Parameters	*R*-Squared	RMS relative error
g_{dn}^{opt}	1	3.5×10^{-4}
Ω_c^{opt}	0.9999	1.8×10^{-3}

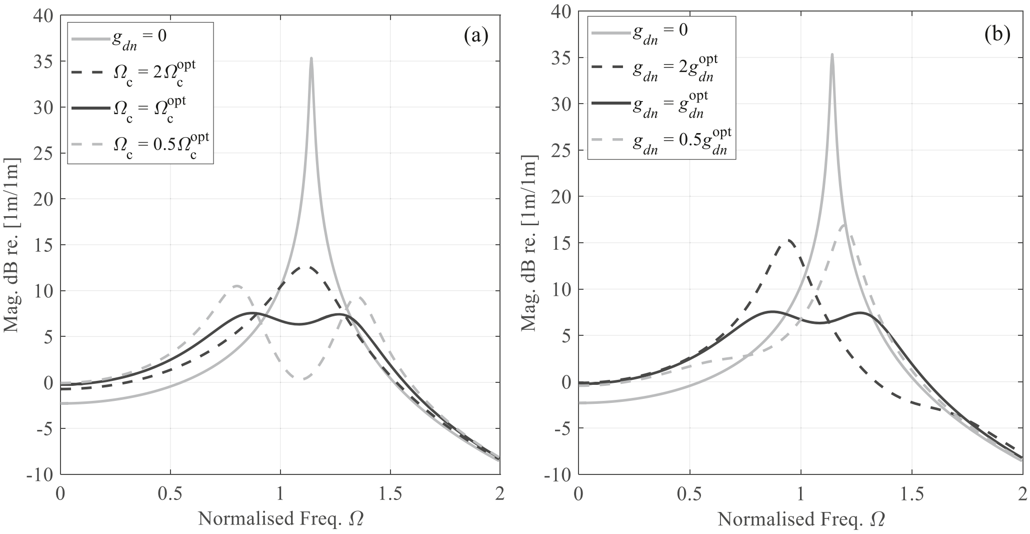

Fig. 2. The performance index against normalised frequency for different (a) cut-off frequencies and (b) feedback gains where the stiffness ratio $\mu = 0.3$ is chosen.

approximation to the numerical results:

$$g_{dn}^{\text{opt}} = 1 + 0.62\mu \tag{13}$$

$$\Omega_c^{\text{opt}} = 0.02 + 0.73\mu^{0.6} - 0.1\mu \tag{14}$$

The goodness of the fitting is given in Table 1 in terms of R-squared and root-mean-square (RMS) relative error.

In the following, numerical simulations are performed to illustrate the control effectiveness and also to examine the tuning law derived in Eqs. (13) and (14). For this numerical study, the stiffness ratio μ is fixed to 0.3 and the proportional feedback gain g_0 is set to zero. Fig. 2 (a) compares the performance index $|x_1/x_d|$ for four different combinations of the control parameters: (i) $g_{dn} = 0$ (control is off); (ii) $g_{dn} = g_{dn}^{\text{opt}}$ and $\Omega_c = 2\Omega_c^{\text{opt}}$; iii) $g_{dn} = g_{dn}^{\text{opt}}$ and $\Omega_c = \Omega_c^{\text{opt}}$ and iv) $g_{dn} = g_{dn}^{\text{opt}}$ and $\Omega_c = 0.5\Omega_c^{\text{opt}}$, whereas Fig. 2 (b) shows the effect when the other parameter g_{dn} deviates from its optimal value by a factor of 2 and 0.5, considering $\Omega_c = \Omega_c^{\text{opt}}$. It can be seen that two peaks with equal amplitude are obtained in accordance with the $\mathbb{H}_\infty$ criterion only when the optimal setting is applied. It is also interesting to note that the DC gain of the performance index i.e. the equivalent static stiffness of the system is dependent on the control parameters. This can be explained with the aid of the equivalent mechanical network shown in Fig. 1 (b). At low frequencies, the ATID-P (assuming $g_0 = 0$) essentially behaves as a spring whose stiffness is $k_m = a^2 k_a / g_d$ in Eq. (6). When g_{dn} is set to zero (control is off), the corresponding stiffness k_m approaches infinity so that k_a represents the whole branch. In such a case, the static stiffness of the system becomes the sum of k_a and k_1. On the other hand, if g_{dn} is non-zero, k_m is finite. This makes the overall stiffness of the ATID-P branch lower than either of the two stiffness k_a or k_m since they are connected in series. Thus, the system becomes softer compared to the case when g_{dn} is set to zero.

Although the stability of the ATID-P is guaranteed because of its full analogy with a mechanical network (given idealised force sensors and actuators are employed and $g_0 > -1$), it is not clear what is the phase margin of this active system when the optimal feedback gains are implemented. In what follows, the open-loop gain of the active system $L = G(j\Omega)H(j\Omega)$ is derived to study phase margin. $G(j\Omega)$ and $H(j\Omega)$represent the normalised frequency response of the control plant and controller, respectively. They are expressed as:

$$G(j\Omega) = \frac{1 - \Omega^2}{(1 - \Omega^2 + \mu)(1 + g_0)} \tag{15}$$

$$H(j\Omega) = \frac{g_{dn}(1 + g_0)}{(\Omega_c{}^2 - \Omega^2 + 2\Omega\Omega_c j)} \tag{16}$$

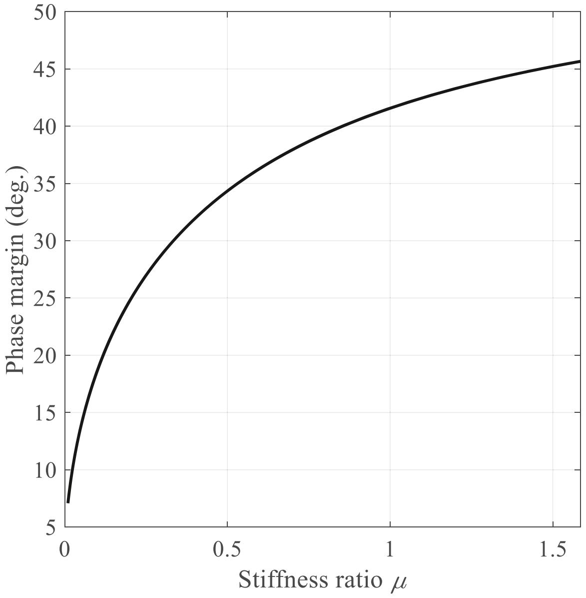

Fig. 3. Phase margin of the SDOF-ATID-P coupled system when the optical settings are applied.

In practice, the ATID-P is implemented in a cascade way. The control plant G in Eq. (15) actually represents the transfer function between the output of the force sensor and the input to the actuator when the control loop with the proportional term is closed, whereas H in Eq. (16) stands for the second-order low-pass filter left in the cascaded controller. This treatment makes sense since the optimal settings of g_{dn} and ω_c in the second-order low-pass filter are derived provided that g_0 is fixed i.e. the proportional control loop is already closed. The phase margin of the optimally configured ATID-P is calculated in three steps: i) identification of the unit gain frequency Ω_c at which the amplitude of the loop gain $L(j\Omega)$ equals to unity; ii) calculation of the phase angle of the loop gain at Ω_c i.e. $\angle L(j\Omega_c)$ and iii) calculation of the phase margin as $PM = \pi + L(j\Omega_c)$.

Fig. 3 plots the phase margin of the coupled system against the stiffness ratio μ when the optimal control parameters are applied. It can be seen that the phase margin increases with an increase in μ. In order to achieve a phase margin greater than 35°, the stiffness of the actuator has to be at least greater than half of the primary system's stiffness. With the proposed ATID-P, the stiffness ratio μ can be effectively adjusted by changing the proportional feedback gain g_0 according to Eq. (7). For example, a large value of μ can be obtained when g_0 falls in the range $(-1, 0]$ where μ increases as g_0 approaches -1. According to Eq. (15), the effective stiffness ratio μ can be estimated in practice by:

$$\mu = \left(\frac{\omega_p}{\omega_z}\right)^2 - 1 = {\Omega_p}^2 - 1 \tag{17}$$

where ω_p and ω_z correspond to the frequencies of the pole and the zero of the control plant respectively, and $\Omega_p$is the normalised frequency of the pole.

In the following, the controller effectiveness of the proportional term is illustrated. Fig. 4 (a) compares the control plant of the considered system when the gain g_0 is set to 0, -0.5 and -0.786, respectively. The effective stiffness ratio μ for these values of g_0 can be calculated based on Eq. (7) and equals 0.3, 0.6 and 1.41. As shown, there exists a pair of complex zeros and a pair of complex poles in the control plant for each scenario. The location of the zeros is invariant with respect to the gain g_0 since it is solely determined by the resonance frequency of the primary structure when the actuator is removed. On the other hand, the location of the poles shifts rightwards when g_0 moves towards to -1. In addition, the magnitude of the control plant is amplified by a factor of $1/(1+g_0)$. In [30], a proportional controller is also considered in order to boost the control performance of integral force feedback controllers. It is implemented as a feedforward term which consequently shifts the zero frequency leftwards while the location of the poles is kept fixed. With the proposed feedback approach, it is opposite i.e. the zero is fixed but the pole increases when increasing the gain g_0.

Fig. 4 (b) plots the open-loop gain of the system for the three values of g_0. The loop gain decreases with a decrease of g_0 (an increase of μ) in the low frequency range. This means that the transmission force at low frequency is less affected when the control is activated. As a consequence, the softening effect induced by the integral force feedback [31,32] becomes less pronounced. In addition, the unit gain frequency at which the phase is smallest increases with a decrease of g_0. This leads to a greater phase margin which is consistent with the phase margin plot in Fig. 3.

Fig. 4 (c) depicts the performance index for the same variation of g_0. The peak values indeed decrease and the static stiffness of the system is less influenced as g_0 approaches -1. It is also interesting to note that the equal peak feature is maintained when a large value of μ is implemented. This demonstrates the validity of the optimal formulae in Eqs. (13) and (14) for a large range of applications.

For the considered values of g_0, the control effectiveness of ATID-P can be compared with that of the modified ATID as in Eq. (4)

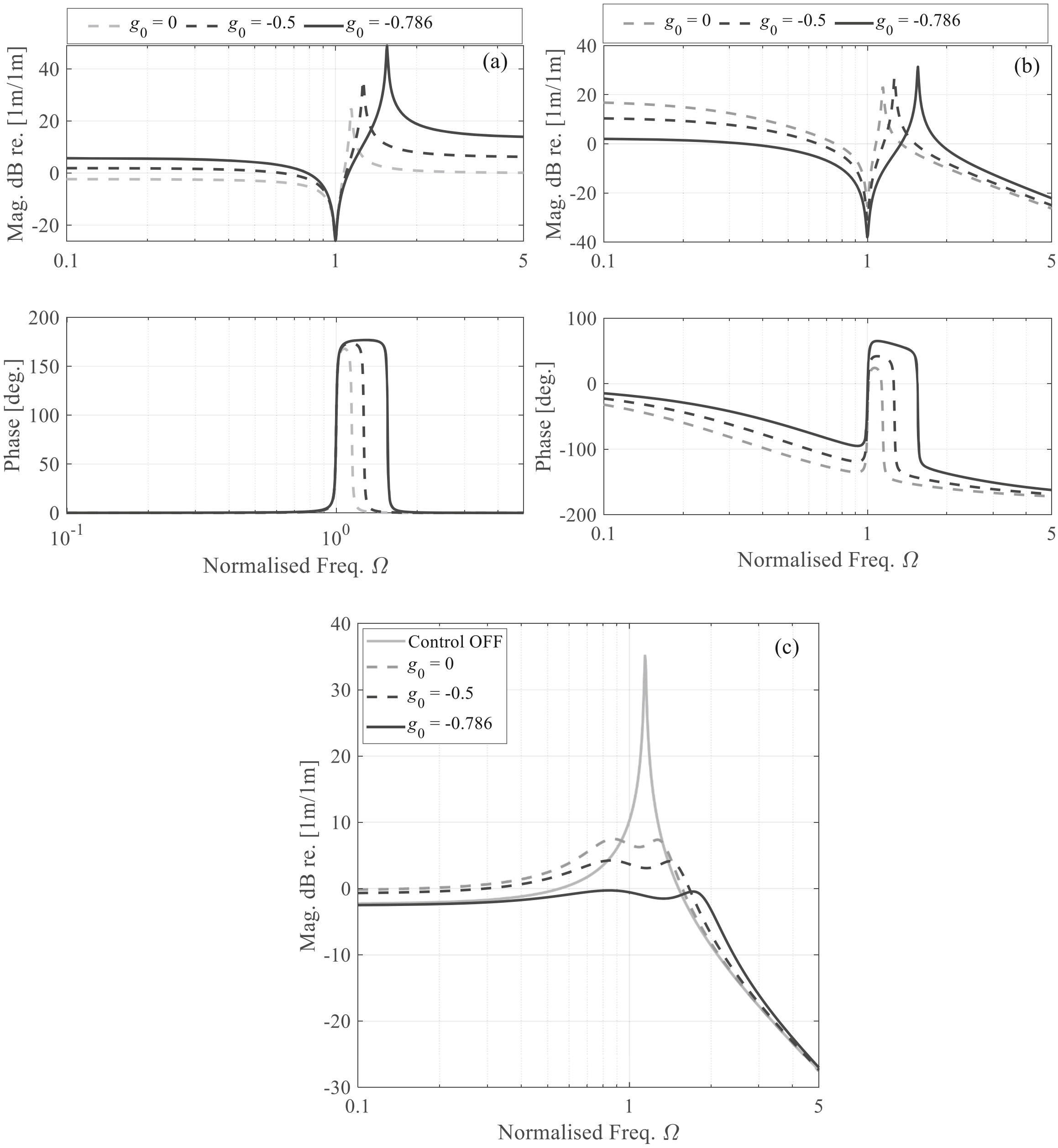

Fig. 4. The frequency response function of (a) the control plant, (b) the open-loop gain and (c) magnitude of the performance index for different values of g_0.

where both first and second order low-pass filters are employed i.e. ATID-S. The cut-off frequency of the low-pass filters used in the ATID-S is one tenth the natural frequency of the primary structure. Two sets of control parameters are considered. For the first case, the gains associated with the first-order and second-order low-pass filters are taken the same as that derived in [23] which means that the influence due to the use of low-pass filters is neglected. In order to account for this influence, these two gains are modified in the second case to retrieve the equal peak property according to the numerical $\mathbb{H}_\infty$ optimisation performed in Appendix B. The resulting performance index of the ATID-P and ATID-S (with and without gain corrections) is compared in Fig. 5. It can be seen that ATID-P always outperforms the ATID-S for the considered values of g_0. The main reason behind the performance difference can be attributed to the different layouts of their equivalent mechanical components as shown in Fig. 1(b) and (d). For ATID-S, the DC gain of the driving-point receptance is derived from Eq. (B.1) by substituting $S = 0$, which reads:

$$\left|\frac{x_1}{x_d}\right|_{S=0}^{\mathrm{ATID-S}} = \frac{{\Omega_c}^2 + \Omega_c g_{sn} + g_{dn}}{{\Omega_c}^2(\mu + 1) + \Omega_c g_{sn} + g_{dn}}. \tag{18}$$

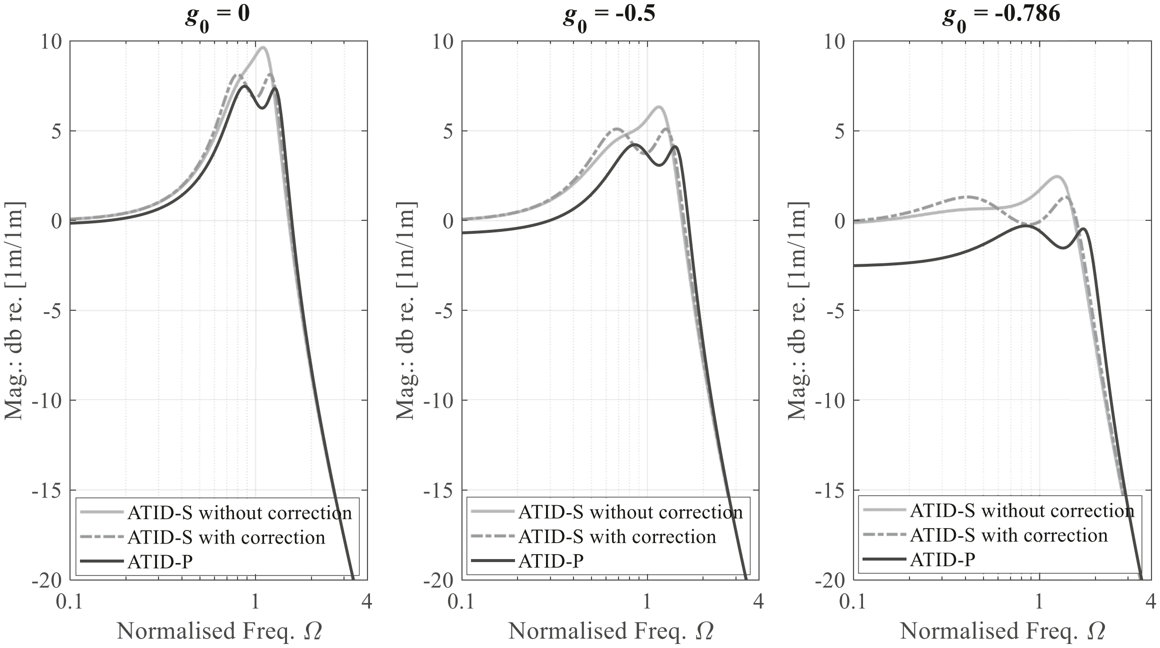

Fig. 5. Control performance comparison for ATID-P and ATID-S (without and with gain corrections).

Since Ω_c is often chosen relatively low for implementing the low-pass filters, the DC gain can be considered as invariant with respect to the control parameters. Consequently, $|x_1/x_d|_{S=0}^{\text{ATID-S}} \approx 1$ is established for different values of μ as shown in Fig. 5 (a)–(c). This makes the minimal maximum value of the cost function hardly able to go below unity when the ATID-S is used.

On the other hand, the DC gain for the ATID-P scenario can be obtained in a similar way from Eq. (12), which is expressed as:

$$\left|\frac{x_1}{x_d}\right|_{S=0}^{\text{ATID-P}} = \frac{{\Omega_c}^2 + g_{dn}}{{\Omega_c}^2(\mu+1) + g_{dn}} \tag{19}$$

In such a case, Ω_c is not negligible anymore which actually makes the DC gain decrease with an increase of μ. For example, the DC gain drops to 0.75 when μ is set to 1.4 as in the case shown in Fig. 5 (c). This opens the door for the $\mathbb{H}_\infty$ algorithm to find a solution for the ATID-P to have the minimal maximum of the cost function smaller than unity as shown in Fig. 5 (c). As such, the outperformance of ATID-P is more visible when μ is relatively large. This also indicates that the ATID-P concept would be preferred in practice as it not only suppresses the low frequency saturation problems but also yields a better control performance in the $\mathbb{H}_\infty$ sense.

Finally, it should be noted that the optimal feedback gains in Eqs. (13) and (14) are derived for an ideal SDOF system, but it is also possible to use them for a specific mode of multi-degree-of-freedom (MDOF) systems as demonstrated in Krenk et al. [33]. In such a scenario, careful calibrations of the system are needed to identify the contributions from non-resonant modes. The non-resonant modes which are lower than the target mode introduce an inertial effect, whereas higher modes bring a quasi-static contribution to the target mode. The calibration procedure of the proposed ATID-P for MDOF systems is left for a future work.

3. Experimental validation

In order to experimentally validate the theoretical analysis, the test bench was prepared, which is shown in Fig. 6. The primary structure is a cantilever aluminium beam with the dimensions 45 cm × 3 cm × 0.3 cm (length*width*thickness). The beam was clamped at one end and excited with two voice coil actuators (*AVM24-10*) at the other end. One of them is used to introduce the disturbance force and the other one is used to deliver the control force. According to the Lorentz law, the force delivered by an ideal voice coil actuator (its mass and damping are neglected) can be regulated by Preumont et al. [31]:

$$f = -2\pi nrBi \tag{20}$$

where i is the input current, B the magnetic flux, $2\pi rn$is the length exposed to the magnetic flux.

Close to the voice coil actuators, an eddy-current sensor (*ECL101*) was installed to measure the tip displacement of the beam. In this study, only the first bending mode of the beam is considered such that the single-mode beam can dynamically represent a linear SDOF system. The block diagram of the control scheme is depicted in Fig. 7. Underneath the control actuator, a force sensor (*PCB 221B02*) is installed in order to measure the transmission force and provide the feedback signal. However, additional damping is induced by the voice coil actuators (the eddy-current effect and air viscous damping effect), which violates the low damping assumption of the primary structure. Thus, a negative damping control loop was implemented in order to eliminate the total inherent damping of the

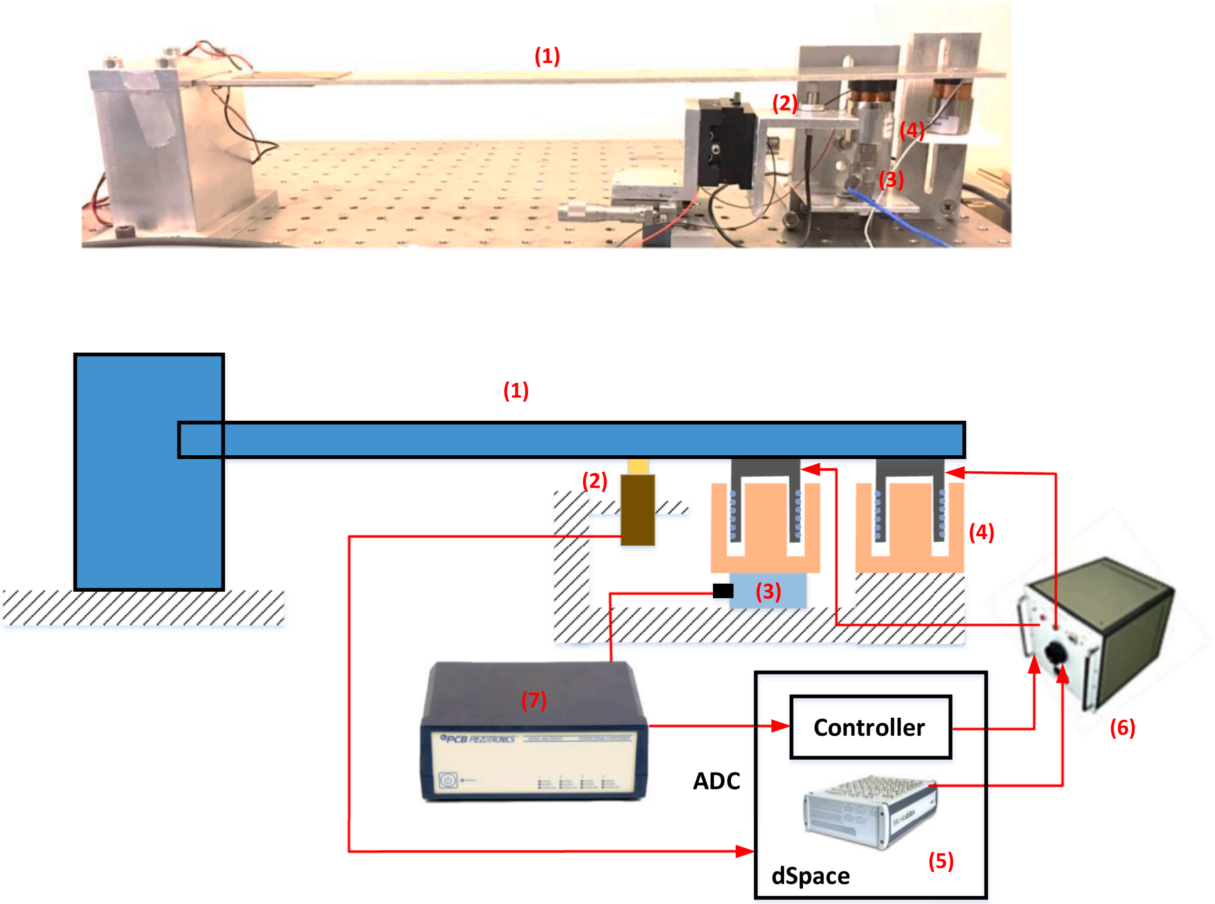

Fig. 6. The experimental test set-up: (1) cantilever beam, (2) eddy-current sensor (ECL101), (3) force sensor (PCB 221B02), (4) voice coil actuator (AVM24-10), (5) MicroLabBox, (6) current amplifier (ADD-45N) and (7) ICP conditioner (PCB 482C05).

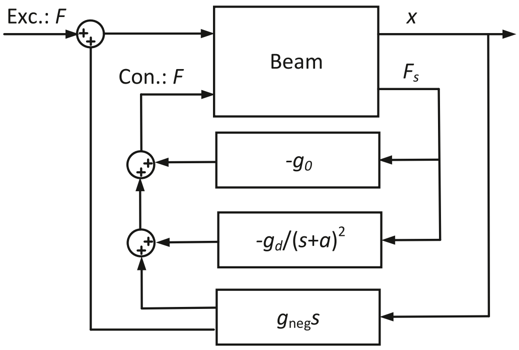

Fig. 7. The configuration scheme of the experimental set-up.

system. This was achieved by positively feeding the tip velocity signal back to drive the voice coil actuators. The velocity signal is obtained by passing the displacement signal measured by the eddy current sensor through a first-order high-pass filter with a corner frequency of 500 Hz. The high-pass filter instead of a pure derivative is used which is mainly to avoid the over-injection of the high-frequency sensor noise. The feedback gain of this negative damping loop is denoted as g_{neg}. Note that the force sensor is placed underneath the magnet of the voice coil actuator which is different to the proposed configuration in Fig. 1 (a). This is done mainly to avoid adding too much weight to the beam. Nevertheless, the actuator actually delivers a pair of reactive force which on one hand acts on the beam and on the other hand on the ground. Therefore, the force sensor in the current configuration measures the same transmission force as it would be in the configuration as indicated in Fig. 1 (a).

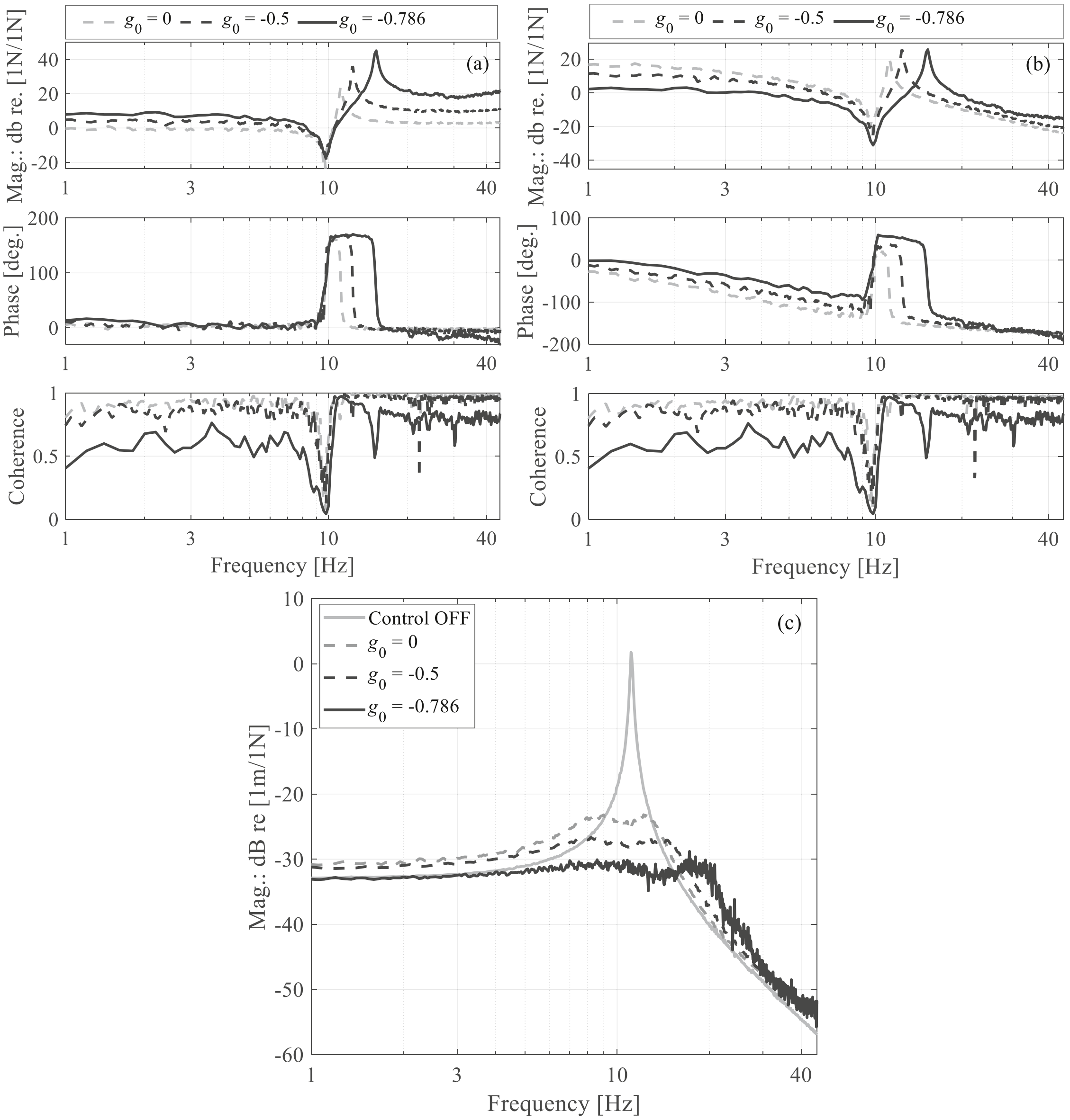

Fig. 8. The frequency response of (a) the control plant, (b) the open loop gain and (c) magnitude of the performance index for different values of g_0.

One can also tell from Fig. 1 (a) that the two actuators and the displacement sensor should be located at the same position. However, this was not the case for the experimental set-up. This imperfection might affect the system identification results and the derivation of the corresponding control parameters provided the transfer function between the ‘control’ actuator and the displacement sensor is noticeably different to that between the ‘disturbance’ actuator and the displacement sensor. It was found that the difference between these two transfer functions is negligible with the current configuration as shown in Fig. 6, which is further evidenced by the experimental results. Therefore, no extra efforts were spent to develop a perfect set-up which is left in a future work for the investigations on MDOF applications.

A *dSpace MicroLabBox* system was used both for the data acquisition and the control implementation. The control scheme was implemented in the *Matlab Simulink* environment and then downloaded to the processor unit of the *MicroLabBox* system. The control scheme was updated at a sampling frequency of 10 kHz, and the measured data were recorded at the same sampling frequency. A current amplifier (*ADD-45N*) was used to drive the voice coil actuators.

The optimal values of the control parameters were derived through 4 steps:

- First, a measurement of the control plant is performed, based on which the locations of the zeros and the poles as well as the DC gain are extracted.

Table 2
Control parameters.

parameters	$g_0 = 0$	$g_0 = -0.492$	$g_0 = -0.786$
μ	0.307	0.604	1.425
ICF	0.82	0.814	0.778
g_d	3652.1	2128.1	1181.6
a	21.34	30.53	47.73
g_{neg}	850	850	850

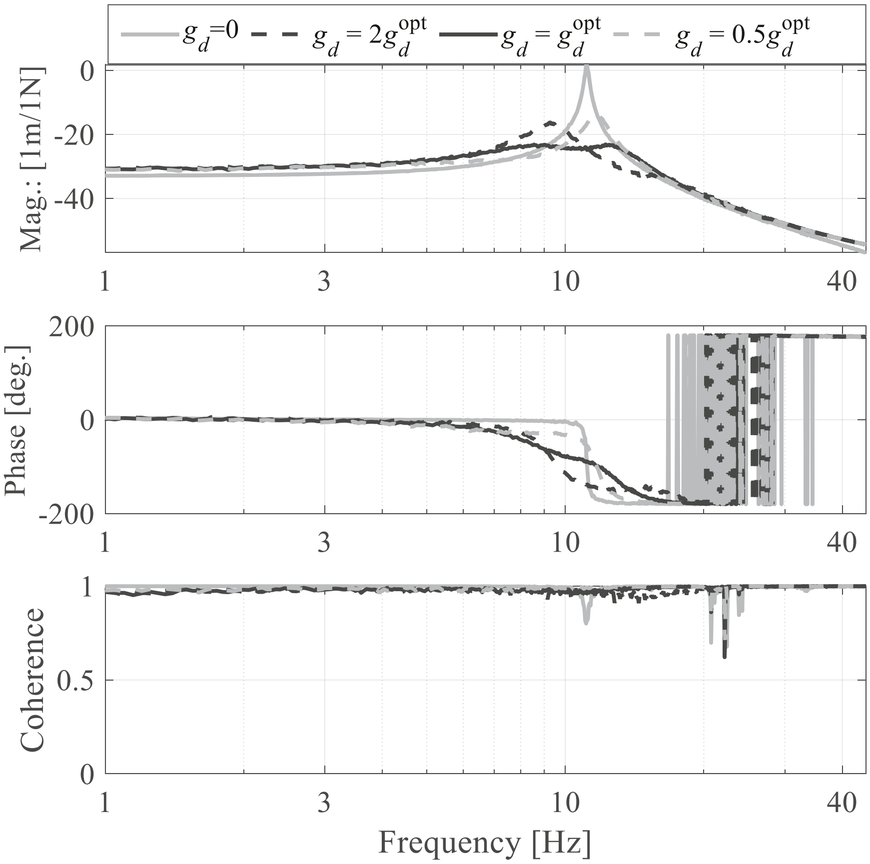

Fig. 9. Comparison of the driving-point receptance when $g_0 = 0$, $a = a_{opt}$ and g_d is varied from 0.5 to 2 times its optimal value.

- The effective stiffness ratio μ was estimated for a fixed value of g_0. This was done by substituting the zero-pole locations identified in the first step into Eq. (17).
- The third step focused on the quantification of the mode interactions between the other structural modes and the targeted mode i.e. the first mode. According to Krenk and Hogsberg [33], the influence of higher modes can be characterised as a quasi-static contribution, which makes the true optimal gains different from those of a SDOF system. This effect can be quantified by comparing the DC gain of the control plants of the equivalent SDOF system with that of a SDOF system. For a SDOF system, the DC gain defined as the response of the control plant at 0 Hz i.e. $G(0)$ is only determined by the parameters μ and g_0 given in Eq. (15). While for the equivalent SDOF system, the DC gain is also influenced by the contributions from the higher modes, which can be simply considered as a gain effect. Therefore, this difference referring to as interaction correction factor (ICF), needs to be multiplied with the derived optimal gains as in Eqs. (13) and (14) in order to eliminate the influence of the mode interactions.
- Finally, the identified stiffness ratio μ, the ICF and the frequency of the zero (corresponding to the resonance of the primary structure when the actuator is removed i.e.ω_1 in Eq. (7)) are substituted into Eqs. (7), (13) and (14) to obtain the optimal feedback gain g_d and cut-off frequency a for implementing the ATID-P controller defined in Eq. (4).

The first set of experiments was conducted to validate the optimal control parameters for different values of g_0. A white noise signal was applied to excite the beam in the vicinity of its first bending mode. The duration of the measurement was set to 200 s.

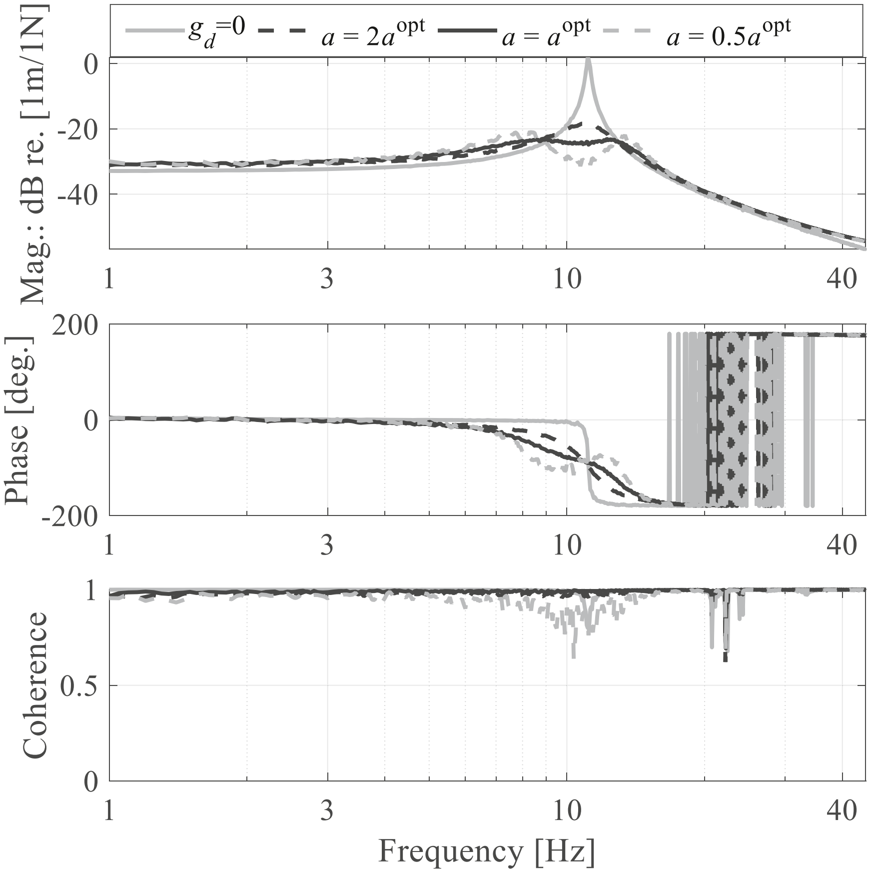

Fig. 10. Comparison of the driving-point receptance when $g_0 = 0$, $g_d = g_d^{\rm opt}$ and a is varied from 0.5 to 2 times its optimal value.

Fig. 8 (a) plots the frequency response of the control plant when g_0 is set to 0, -0.5 and -0.786, respectively. The stiffness ratio, ICF and the optimal control parameters are summarised in Table 2. Note that the coherence of the control plant is relatively low when g_0 is set to -0.786. This is because the magnitude of the control plant is amplified by a factor of $1/(1+g_0)$, and the input disturbance force has to be limited to avoid an overwhelming response around the resonance frequency. As a consequence, the signal-to-noise ratio is low at other frequencies leading to a low coherence. Nevertheless, the optimal control parameters can still be accurately estimated. With these optimal controllers, the open loop gains are shown in Fig. 8 (b). It is found that the phase margin matches very well the theoretical value in Fig. 3. Finally, the control performance is examined. Fig. 8 (c) depicts the driving-point receptance (the transfer function between the disturbance force and the measured tip displacement). As expected, a better control effectiveness is achieved when g_0 approaches -1. The comparison between Figs. 8 and 4 shows that the experimental results are in a good accordance with the theoretical analysis.

Next, the influence of the control parameters' variation is investigated. Fig. 10 compares the driving-point receptance, where g_0 is set to zero, the cut-off frequency a is set to its optimal value (14) and the feedback gain g_d is varied from 0.5 to 2 times its optimal value (13). On the other hand, Fig. 9 investigates the effect of the cut-off frequency a which is varied from 0.5 to 2 times its optimal value, while g_0 is set to zero and g_d is set to its optimal value. The obtained experimental results are in a good accordance with the theoretical predictions in Fig. 2 (a) and (b). The equal-peak feature is obtained when the optimal value of the control parameters is implemented.

The last set of experiments examines the control effectiveness of different controllers as in Fig. 5. Here, the cut-off frequency of the low-pass filter of the ATID-S is set to 1 Hz. Two scenarios are considered where the corrections for the control gains are either implemented or not. The driving-point receptances are compared in Fig. 11, where the results corresponding to the ATID-P are also superimposed. It can be seen that the ATID-P always outperforms the ATID-S for the considered values of g_0, and a visible degradation of the ATID-S's control effectiveness is observed when the corrections due to the use of low-pass filters are not implemented.

4. Conclusion

This paper discusses the practical applicability of a modified active inerter-damper system, the ATID-P, realised using a pair of collocated actuator and force sensor. The controller consists of a second-order low-pass filter and a proportional term. The equivalent mechanical model of the controller's components is derived in order to illustrate the influence of the active control system on the

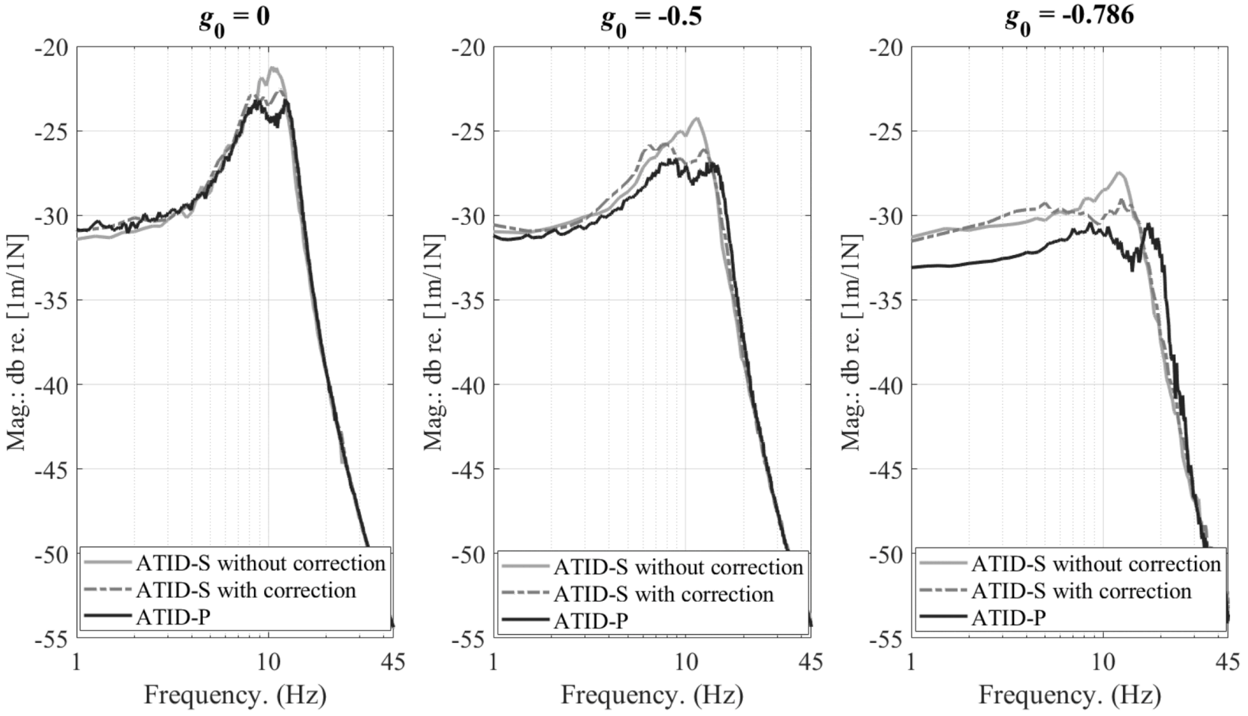

Fig. 11. Control performance comparison for ATID-P and ATID-S (without and with corrections).

primary system. The second-order low-pass filter was found to be equivalent to a pure mechanical network which comprises an inerter, a spring and a damper connected in parallel, and the proportional term plays the same role as a mechanical spring connected in series with the inherent actuator spring. Simple expressions are derived based on the $\mathbb{H}_\infty$ optimisation criterion which aims to minimise the maximal response of the driving-point receptance of the system. It is shown that the performance of the ATID-P is governed by the stiffness ratio between the chosen actuator and the primary structure. By cascading the proportional controller, a relatively large stiffness ratio can be implemented given that the associated gain is properly tuned. This does not only improve the achievable vibration mitigation performance but also increases the phase margin. The numerical study was also experimentally validated. The obtained results were found to be in excellent agreement. With these results, one can envision to develop a simple analogue electronic control system for a collocated actuator-force sensor pair such that the resulting active inerter-based damper would be compact enough for smart structure applications.

CRediT authorship contribution statement

Guoying Zhao: Conceptualization, Methodology, Investigation, Validation, Writing – original draft. **Ahmad Paknejad:** Writing – review & editing. **Ghislain Raze:** Software, Formal analysis, Writing – review & editing. **Arnaud Deraemaeker:** Writing – review & editing. **Gaetan Kerschen:** Supervision, Writing – review & editing. **Christophe Collette:** Supervision, Writing – review & editing.

Declaration of Competing Interest

The authors declare that they have no conflict of interest.

Acknowledgments

The financial supports from Wal’innov (MAVERIC project 1610122) , F.R.S.-FNRS (IGOR project F453617F) and The Innovation and Induction of Disciplines in Higher Education Institutions (111 project B20062) are gratefully acknowledged.

Appendix A

In this appendix, it is shown that the systems sketched in Fig. 1 (a) and (b) are dynamically equivalent, or, in other words, the networks shown in Fig. A.1 (a) and (b) are equivalent.

Fig. A.1 (b) depicts a pure mechanical system which consists of several springs and dashpots as well as an inerter. Under the excitation force denoted by F, the governing equations of this system can be written as:

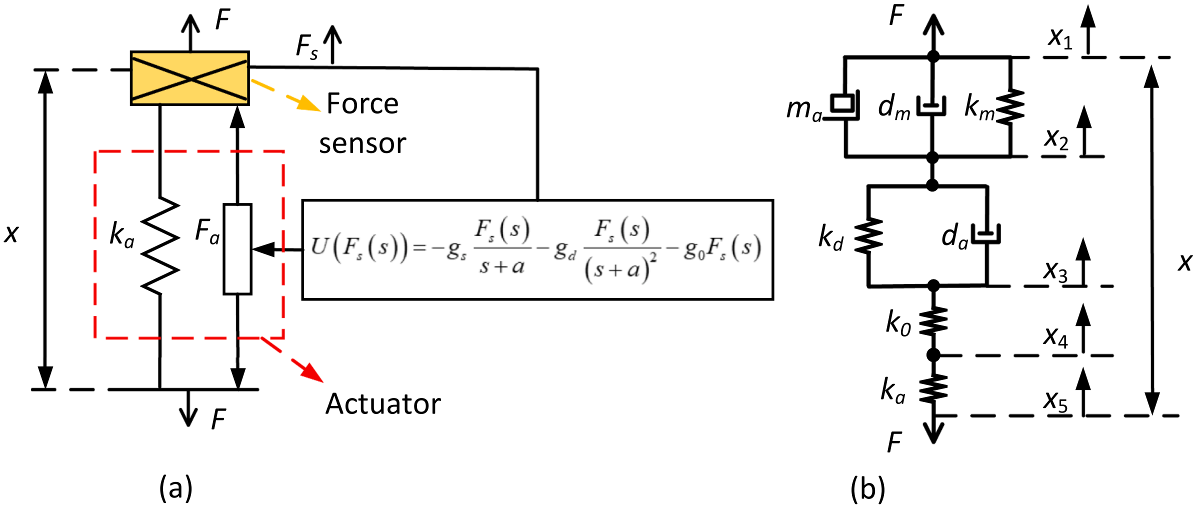

Fig. A.1. (a) the sketch of the active system and (b) its mechanical representative.

$$F = -m_a\left(\ddot{x}_1 - \ddot{x}_2\right) - d_m\left(\dot{x}_1 - \dot{x}_2\right) - k_m(x_1 - x_2) \tag{A.1}$$

$$F = -d_a\left(\dot{x}_2 - \dot{x}_3\right) - k_d(x_2 - x_3) \tag{A.2}$$

$$F = -k_0(x_3 - x_4) \tag{A.3}$$

$$F = -k_a(x_4 - x_5) \tag{A.4}$$

Expressing the relative motion in terms of the transmission force F, Eqs. (A.1)–(A.4) can be rewritten as:

$$x_1 - x_2 = \frac{-F}{m_a s^2 + d_m s + k_m} \tag{A.5}$$

$$x_2 - x_3 = \frac{-F}{d_a s + k_d} \tag{A.6}$$

$$x_3 - x_4 = -\frac{F}{k_0} \tag{A.7}$$

$$x_4 - x_5 = -\frac{F}{k_a} \tag{A.8}$$

Summing up Eqs. (A.5)–(A.8) and multiplying both sides with k_a, yields:

$$k_a(x_1 - x_5) = \frac{-k_a F}{m_a s^2 + d_m s + k_m} - \frac{k_a F}{d_a s + k_d} - \frac{k_a F}{k_0} - F \tag{A.9}$$

According to the control law, the governing equations of the system shown in Fig. A.1(a) can be expressed as:

$$F = -g_s \frac{F_s(s)}{s + a} - g_d \frac{F_s(s)}{(s + a)^2} - g_0 F_s(s) - k_a x \tag{A.10}$$

where $x = x_1 - x_5$ represents the relative displacement across the active inerter damper and $F_s = F$.

Comparing Eq. (A.9) with Eq. (A.10) and one can find the equivalence between systems shown in Fig. A.1(a) and (b). The feedback gains and their corresponding mechanical components are thus related by Eq. (A.11):

$$d_a = \frac{k_a}{g_s}, k_d = \frac{a k_a}{g_s}, m_a = \frac{k_a}{g_d}, d_m = \frac{2 a k_a}{g_d}, k_m = \frac{a^2 k_a}{g_d}, k_0 = \frac{k_a}{g_0} \tag{A.11}$$

Appendix B

In this part, the $\mathbb{H}_\infty$ optimisation of ATID-S is performed. The normalised driving-point receptance of the primary structure when ATID-S is implemented can be derived as:

$$\frac{x_1}{x_d} = \frac{S^2 + (2\Omega_c + g_{sn})S + \Omega_c g_{sn} + {\Omega_c}^2 + g_{dn}}{S^4 + (2\Omega_c + g_{sn})S^3 + \left(1 + {\Omega_c}^2 + g_{dn} + \mu + \Omega_c g_{sn}\right)S^2 + (2\Omega_c(\mu + 1) + g_{sn})S + {\Omega_c}^2(\mu + 1) + \Omega_c g_{sn} + g_{dn}} \tag{B.1}$$

and its magnitude is given as:

$$\left|\frac{x_1}{x_d}\right| = \frac{\sqrt{\Omega^4 + \left((g_{sn} + \Omega_c)^2 + {\Omega_c}^2 - 2g_{dn}\right)\Omega^2 + \left(g_{sn}\Omega_c + {\Omega_c}^2 + g_{dn}\right)^2}}{\sqrt{2\mu\left(\Omega^2 - 1\right)\left(\left(\Omega^2 - {\Omega_c}^2\right)g_{dn} - \left(\Omega^2 + {\Omega_c}^2\right)\left(\Omega^2 + g_{sn}\Omega_c + {\Omega_c}^2\right)\right) + \left(\Omega^2 - 1\right)^2 A + B}} \tag{B.2}$$

where $A = (g_{dn})^2 + (-2\Omega^2 + 2g_{sn}\Omega_c + 2{\Omega_c}^2)g_{dn} + (\Omega^2 + {\Omega_c}^2)(\Omega^2 + (g_{dn} + \Omega_c)^2)$, $S = s/\omega_1$ is the normalised Laplace variable, $\Omega = S/j$ is the normalised frequency and $B = (\Omega^2 + {\Omega_c}^2)^2\mu^2$.

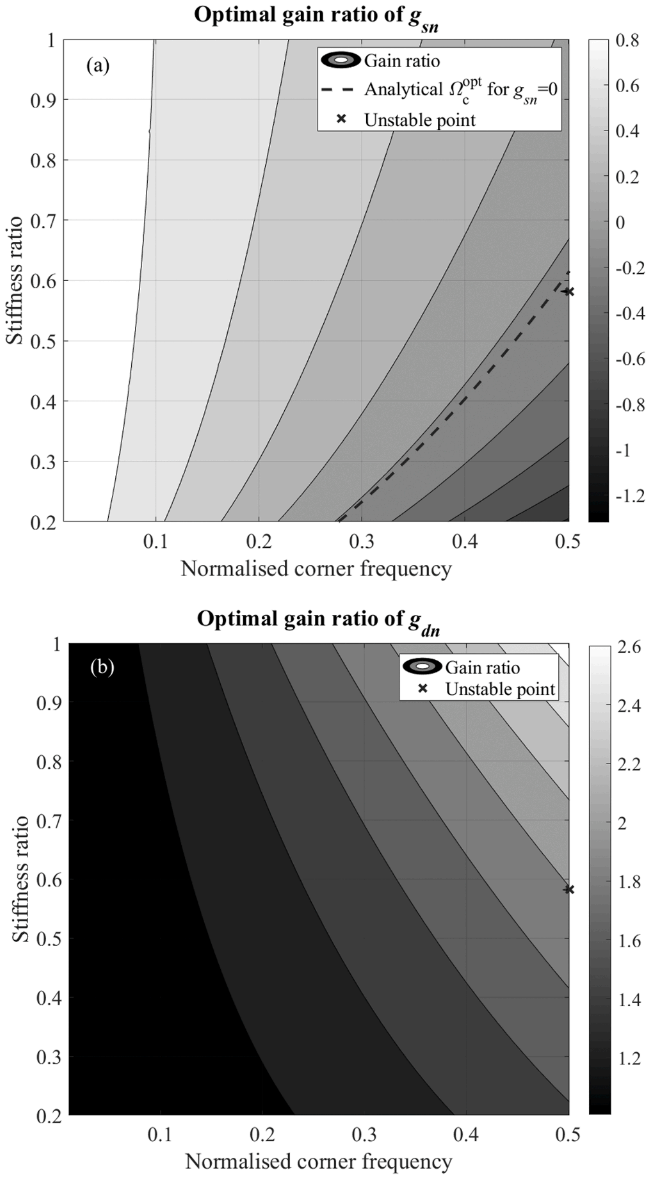

Fig. B.1. Gain ratio between the numerically and analytically obtained values for (a) g_{sn}^{opt} and (b) g_{dn}^{opt}.

A numerical $\mathbb{H}_\infty$ optimisation is performed where the optimal settings of g_{sn} and g_{dn} are derived given μ and Ω_c are fixed. In order to better understand these numerically obtained optimal values, they are compared with the analytically derived counterparts in Zhao et al. [23] where pure integrators are employed i.e. Ω_c is set to zero. Fig. B.1 (a) and (b) plot the ratio between the numerically and analytically obtained values for g_{sn}^{opt} and g_{dn}^{opt} against μ and Ω_c, respectively.

When Ω_c is relatively small, it can be seen that the analytically obtained optimal settings derived for the case where perfect integrators are used [23] can still hold. This implies that these closed-form expressions could be still applicable for high-frequency applications since it allows to choose a relatively high cut-off frequency which helps limit the low frequency amplification but still remains negligible compared with the resonance frequency to be damped. However, this is not case for low-frequency applications for example the active seismic isolation systems used for gravitational wave detections, the resonance frequency of which is often very low [34,35]. In such a case, the cut-off frequency of the low-pass filters is often very close to the resonance frequency i.e. Ω_c is relatively large whereas a dramatic correction is needed for the control parameters. Especially for g_{sn}, it even undergoes a change of sign from positive to negative values. This occurs because the use of a second-order low-pass filter already introduces an additional pair of spring and dashpot in parallel with the desired inerter. The corresponding stiffness and damping are unfortunately more than needed for fulfilling the $\mathbb{H}_\infty$ optimisation criterion. Therefore, a negative gain of the first-order low-pass filter which provides a pair of negative stiffness and damping is sought aiming to compensate the inherent stiffness and damping associated with the second-order low-pass filter. For such scenarios the first-order low-pass filter may not be needed as a second-order low-pass filter with a proper tuning might be already good enough. In addition, the unconditional stability feature might be compromised when a negative feedback gain is used. For example, the system becomes unstable when the derived optimal values are used for $\mu = 0.582$, $\Omega_c = 0.5$, as indicated by the cross marker in Fig. B.1(a). The dependence of Ω_c^{opt} on μ for the ATID-P is also superimposed on Fig. B.1(a). It is seen that it divides the map into two zones: g_{sn}^{opt} is positive or negative for a given pair of Ω_c and μ.

References

[1] F.Y. Wang, Y. Gao, Advanced Studies of Flexible Robotic Manipulators, World Scientific, 2003, https://doi.org/10.1142/5290.

[2] M. Darecki, C. Edelstenne, T. Enders, E. Fernandez, P. Hartman, J.P. Herteman, M. Kerkloh, I. King, P. Ky, M. Mathieu, G. Orsi, G. Schotman, C. Smith, J. D. Wörner, Flightpath 2050, Flightpath 2050, Eur. Vis. Aviat. (2011) 28, https://doi.org/10.2777/50266.

[3] E.O. Ayorinde, G.B. Warburton, Minimizing structural vibrations with absorbers, Earthq. Eng. Struct. Dyn. 8 (1980) 219–236, https://doi.org/10.1002/eqe.4290080303.

[4] S.V. Bakre, R.S. Jangid, Optimum parameters of tuned mass damper for damped main system, Struct. Control Health Monit. 14 (2007) 448–470, https://doi.org/10.1002/stc.166.

[5] W. Ma, Y. Yang, J. Yu, General routine of suppressing single vibration mode by multi-DOF tuned mass damper: application of three-DOF, Mech. Syst. Signal Process. 121 (2019) 77–96, https://doi.org/10.1016/j.ymssp.2018.11.010.

[6] M.D. Christie, S. Sun, L. Deng, D.H. Ning, H. Du, S.W. Zhang, W.H. Li, A variable resonance magnetorheological-fluid-based pendulum tuned mass damper for seismic vibration suppression, Mech. Syst. Signal Process. 116 (2019) 530–544, https://doi.org/10.1016/j.ymssp.2018.07.007.

[7] M.M. Americano da Costa, D.A. Castello, C. Magluta, N. Roitman, On the optimal design and robustness of spatially distributed tuned mass dampers, Mech. Syst. Signal Process. 150 (2021), 107289, https://doi.org/10.1016/j.ymssp.2020.107289.

[8] J.P. Den Hartog, Mechanical Vibrations, Dover Publications, 1985. http://books.google.be/books?id=-Pu5YlgY4QsC.

[9] M.C. Smith, Synthesis of mechanical networks: the inerter, IEEE Trans. Automat. Contr. 47 (2002) 1648–1662, https://doi.org/10.1109/TAC.2002.803532.

[10] M.Z.Q. Chen, C. Papageorgiou, F. Scheibe, F.C. Wang, M. Smith, The missing mechanical circuit element, IEEE Circuits Syst. Mag. 9 (2009) 10–26, https://doi.org/10.1109/MCAS.2008.931738.

[11] I.F. Lazar, S.A. Neild, D.J. Wagg, Performance analysis of cables with attached tuned-inerter-dampers, in: Conference Proceedings of the Society for Experimental Mechanics Series, 2015, pp. 433–441, https://doi.org/10.1007/978-3-319-15248-6_44.

[12] I.F. Lazar, S.A. Neild, D.J. Wagg, Vibration suppression of cables using tuned inerter dampers, Eng. Struct. 122 (2016) 62–71, https://doi.org/10.1016/j.engstruct.2016.04.017.

[13] P. Brzeski, T. Kapitaniak, P. Perlikowski, Novel type of tuned mass damper with inerter which enables changes of inertance, J. Sound Vib. 349 (2015) 56–66, https://doi.org/10.1016/j.jsv.2015.03.035.

[14] C. Paulitsch, P. Gardonio, S.J. Elliott, Active vibration control using an inertial actuator with internal damping, J. Acoust. Soc. Am. 119 (2006) 2131–2140, https://doi.org/10.1121/1.2141228.

[15] N. Alujević, G. Zhao, B. Depraetere, P. Sas, B. Pluymers, W. Desmet, Optimal vibration control using inertial actuators and a comparison with tuned mass dampers, J. Sound Vib. 333 (2014) 4073–4083, https://doi.org/10.1016/j.jsv.2014.04.038.

[16] M. Zilletti, Feedback control unit with an inerter proof-mass electrodynamic actuator, J. Sound Vib. 369 (2016) 16–28, https://doi.org/10.1016/j.jsv.2016.01.035.

[17] N. Alujević, D. Čakmak, H. Wolf, M. Jokić, Passive and active vibration isolation systems using inerter, J. Sound Vib. 418 (2018) 163–183, https://doi.org/10.1016/j.jsv.2017.12.031.

[18] C. Papageorgiou, N.E. Houghton, M.C. Smith, Experimental testing and analysis of inerter devices, J. Dyn. Syst. Meas. Control. 131 (2009), 011001, https://doi.org/10.1115/1.3023120.

[19] S.J. Swift, M.C. Smith, A.R. Glover, C. Papageorgiou, B. Gartner, N.E. Houghton, Design and modelling of a fluid inerter, Int. J. Control. 86 (2013) 2035–2051, https://doi.org/10.1080/00207179.2013.842263.

[20] J. Høgsberg, M.L. Brodersen, S. Krenk, Resonant passive – active vibration absorber with integrated force feedback control, Smart Mater. Struct. 25 (2016), https://doi.org/10.1088/0964-1726/25/4/047001, 0.

[21] C. Collette, S. Chesné, Robust hybrid mass damper, J. Sound Vib. 375 (2016) 19–27, https://doi.org/10.1016/j.jsv.2016.04.030.

[22] S. Chesné, A. Milhomem, C. Collette, Enhanced damping of flexible structures using force feedback, J. Guid. Control Dyn. 39 (2016) 1654–1658, https://doi.org/10.2514/1.G001620.

[23] G.. Zhao, G. Raze, A. Paknejad, A. Deraemaeker, G. Kerschen, C. Collette, Active tuned inerter-damper for smart structures and its $\mathbb{H}\infty$ optimisation, Mech. Syst. Signal Process. 129 (2019) 470–478, https://doi.org/10.1016/j.ymssp.2019.04.044.

[24] G. Zhao, G. Raze, A. Paknejad, A. Deraemaeker, G. Kerschen, C. Collette, Active nonlinear inerter damper for vibration mitigation of Duffing oscillators, J. Sound Vib. 473 (2020), 115236, https://doi.org/10.1016/j.jsv.2020.115236.

[25] G. Zhao, G. Raze, A. Paknejad, A. Deraemaeker, G. Kerschen, C. Collette, Active nonlinear energy sink using force feedback under transient regime, Nonlinear Dyn. 102 (2020) 1319–1336, https://doi.org/10.1007/s11071-020-06000-y.

[26] M. Neubauer, J. Wallaschek, Vibration damping with shunted piezoceramics: fundamentals and technical applications, Mech. Syst. Signal Process. 36 (2013) 36–52, https://doi.org/10.1016/j.ymssp.2011.05.011.

[27] A. Preumont, Vibration control of active structures, 2018. 10.1007/978-94-007-2033-6.

[28] G. Zhao, N. Alujević, B. Depraetere, P. Sas, Dynamic analysis and $\mathbb{H}2$ optimisation of a piezo-based tuned vibration absorber, J. Intell. Mater. Syst. Struct. 26 (2015) 1995–2010, https://doi.org/10.1177/1045389X14546652.

[29] G. Zhao, N. Alujevia, B. Depraetere, G. Pinte, P. Sas, Adaptive-passive control of structure-borne noise of rotating machinery using a pair of shunted inertial actuators, J. Intell. Mater. Syst. Struct. 27 (2016) 1584–1599, https://doi.org/10.1177/1045389X15600080.

[30] Y.R. Teo, A.J. Fleming, Optimal integral force feedback for active vibration control, J. Sound Vib. 356 (2015) 20–33, https://doi.org/10.1016/j.jsv.2015.06.046.

[31] A. Preumont, J.P. Dufour, C. Malekian, Active damping by a local force feedback with piezoelectric actuators, J. Guid. Control Dyn. 15 (1992) 390–395, https://doi.org/10.2514/3.20848.

[32] G. Zhao, A. Paknejad, A. Deraemaeker, C. Collette, $\mathbb{H}\infty$ optimisation of an integral force feedback controller, J. Vib. Control 25 (2019) 2330–2339, https://doi.org/10.1177/1077546319853165.

[33] S. Krenk, J. Hogsberg, Tuned resonant mass or inerter-based absorbers: unified calibration with quasi-dynamic flexibility and inertia correction, Proc. R. Soc. A Math. Phys. Eng. Sci. 472 (2016), https://doi.org/10.1098/rspa.2015.0718.

[34] F. Matichard, B. Lantz, K. Mason, R. Mittleman, B. Abbott, S. Abbott, E. Allwine, S. Barnum, J. Birch, S. Biscans, D. Clark, D. Coyne, D. DeBra, R. DeRosa, S. Foley, P. Fritschel, J.A. Giaime, C. Gray, G. Grabeel, J. Hanson, M. Hillard, J. Kissel, C. Kucharczyk, A. Le Roux, V. Lhuillier, M. Macinnis, B. O'Reilly, D. Ottaway, H. Paris, M. Puma, H. Radkins, C. Ramet, M. Robinson, L. Ruet, P. Sareen, D. Shoemaker, A. Stein, J. Thomas, M. Vargas, J. Warner, Advanced LIGO two-stage twelve-axis vibration isolation and positioning platform. Part 1: design and production overview, Precis. Eng. 40 (2015) 273–286, https://doi.org/10.1016/j.precisioneng.2014.09.010.

[35] G. Zhao, B. Ding, J. Watchi, A. Deraemaeker, C. Collette, Experimental study on active seismic isolation using interferometric inertial sensors, Mech. Syst. Signal Process. 145 (2020), 106959, https://doi.org/10.1016/j.ymssp.2020.106959.